How to cite: *Angew. Chem. Int. Ed.* **2021**, *60*, 20407–20416
International Edition: doi.org/10.1002/anie.202103641
German Edition: doi.org/10.1002/ange.202103641

VIP **Cluster Compounds** *Very Important Paper*

Structural Changes during the Growth of Atomically Precise Metal Oxido Nanoclusters from Combined Pair Distribution Function and Small-Angle X-ray Scattering Analysis

Andy S. Anker, Troels Lindahl Christiansen, Marcus Weber, Martin Schmiele, Erik Brok, Emil T. S. Kjær, Pavol Juhás, Rico Thomas, Michael Mehring, and Kirsten M. Ø. Jensen**

Abstract: *The combination of in situ pair distribution function (PDF) analysis and small-angle X-ray scattering (SAXS) enables analysis of the formation mechanism of metal oxido nanoclusters and cluster–solvent interactions as they take place. Herein, we demonstrate the method for the formation of clusters with a $[Bi_{38}O_{45}]$ core. Upon dissolution of crystalline $[Bi_6O_5(OH)_3(NO_3)_5]\cdot 3H_2O$ in DMSO, an intermediate rapidly forms, which slowly grows to stable $[Bi_{38}O_{45}]$ clusters. To identify the intermediate, we developed an automated modeling method, where smaller $[Bi_xO_y]$ structures based on the $[Bi_{38}O_{45}]$ framework are tested against the data. $[Bi_{22}O_{26}]$ was identified as the main intermediate species, illustrating how combined PDF and SAXS analysis is a powerful tool to gain insight into nucleation on an atomic scale. PDF also provides information on the interaction between nanoclusters and solvent, which is shown to depend on the nature of the ligands on the cluster surface.*

Introduction

The design of new functional materials relies on understanding the fundamental chemical reactions that govern material formation and growth. In inorganic and materials chemistry, we are still challenged in describing these processes on an atomic level,[1] as studies of nucleation and growth phenomena are challenging. In recent years, atomically precise metal oxido nanoclusters of titanium,[2] cerium[3] and bismuth have been intensively studied due to their wide range of applications, for example, for photocatalysis,[2] oxygen storage,[3] in medicine,[4] as radiopaque materials[4b,5] or as building blocks for advanced catalysts.[6] Apart from their technological relevance understanding the solution chemistry of such metal oxido clusters on an atomic and molecular scale can open new opportunities for synthesizing nanoscale metal oxides in a controlled manner.[6,7]

We have in recent years focused on the chemistry of bismuth oxido clusters and have synthesized a range of differently sized molecules and nanoclusters.[4a,8] These nanoclusters are generally composed of a bismuth oxido core $[Bi_xO_y]^{z+}$ of varying nuclearity and charge, and anionic ligands (e.g. nitrate, carboxylates, aryl sulfonates, silanolates) for charge compensation. In the following, we will refer to the structures of the nanoclusters as $[Bi_xO_y]$ neglecting charge and ligand shell. The nanoclusters can be considered built from $[Bi_6O_8]$ units which share edges (as defined from the octahedra formed from Bi atoms, Figure 1 A,B) to form larger clusters. These clusters represent cut-outs of the fluorite-type structure which constitutes the basis of δ- and β-Bi_2O_3.[6,9] For example, the $[Bi_{22}O_{26}]$ cluster[8e] (Figure 1 C) is composed of 6 of these basic motifs and the $[Bi_{38}O_{45}]$ cluster[4a] (Figure 1 D) of 13. Similar structures are seen in metal oxido clusters of other large cations such as $[Ce_{22}O_{24}]$,[10] $[Ce_{38}O_{54}]$,[3a] $[U_{38}O_{56}]$,[11] and $[Pu_{38}O_{56}]$.[12] The $[M_6O_x]$ building block, where M is a metal, is therefore anticipated to play an important role in the cluster growth, however, an understanding of the mechanisms controlling this process in solution is still missing. In situ investigations have shed light on cluster reactions in solution, and the cluster growth from $[Bi_6O_8]$ to $[Bi_{38}O_{45}]$ has previously been investigated with electrospray ionization mass spectrometry (ESI-MS).[13] A variety of bismuth oxido clusters were observed during the reaction, but $[Bi_6O_8]$, $[Bi_{22}O_{27}]$ and $[Bi_{38}O_{45}]$ clusters were

[*] A. S. Anker, Dr. T. L. Christiansen, E. T. S. Kjær, Dr. K. M. Ø. Jensen
Department of Chemistry and Nano-Science Center
University of Copenhagen
Universitetsparken 5, 2100 Copenhagen E (Denmark)
E-mail: kirsten@chem.ku.dk
Dr. M. Weber, R. Thomas, Prof. Dr. M. Mehring
Fakultät für Naturwissenschaften, Institut für Chemie
Professur Koordinationschemie, Technische Universität Chemnitz
Strasse der Nationen 62, 09111 Chemnitz (Germany)
and
Center for Materials, Architectures and Integration of Nanomembranes (MAIN)
Rosenbergstrasse 6, 09126 Chemnitz (Germany)
E-mail: michael.mehring@chemie.tu-chemnitz.de
Dr. M. Schmiele, Dr. E. Brok
Niels Bohr Institute and Nano-Science Center
University of Copenhagen
Universitetsparken 5, 2100 Copenhagen E (Denmark)
Dr. P. Juhás
Computational Science Initiative, Brookhaven National Laboratory
98 Rochester Street, Upton, NY 11973 (USA)
Supporting information and the ORCID identification number(s) for the author(s) of this article can be found under: https://doi.org/10.1002/anie.202103641.

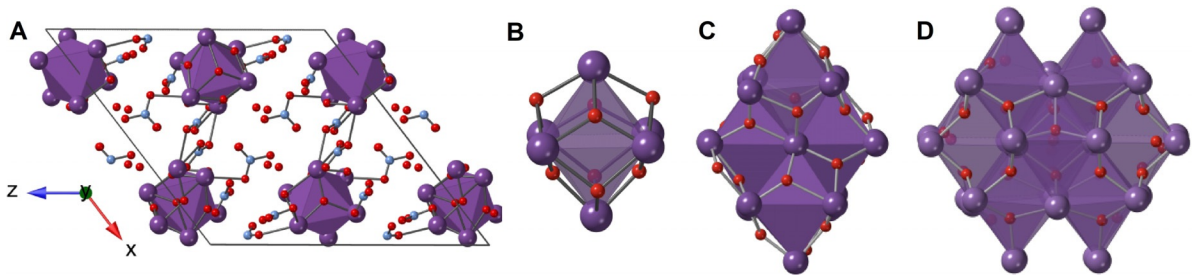

Figure 1. A) Structure of crystalline $[Bi_6O_5(OH)_3(NO_3)_5]\cdot 3H_2O$.[8a] Hydrogen atoms have been omitted for clarity. B) An octahedral $[Bi_6O_8]$ unit. C) The $[Bi_{22}O_{26}]$[8e] cluster structure. D) The $[Bi_{38}O_{45}]$[4a] cluster structure. In all structures, bismuth is shown in purple, oxygen in red, and nitrogen in blue.

identified as particularly stable, which agrees well with other cluster studies.[3a,9a,11,12,14] From these experiments, Sattler et al.[13] proposed that cluster growth happens through di- or oligomerization reactions and rearrangement processes, with cluster growth starting from hexanuclear metal oxido clusters. Based on the ESI-MS findings, as well as on knowledge on crystal structures of polynuclear clusters (containing 6–10 Bi atoms), the reaction is expected to proceed through intermediate species formed by addition of bismuth containing fragments of dissociated $[Bi_6O_8]$ units to the cluster core.[15] However, while mass spectrometry gives information about the atomic composition of the species present during growth, the evolution of the atomic structure in solution is yet to be unraveled.

The molecular structures of many bismuth oxido nanoclusters are well known, as these can be characterized with single crystal diffraction. The structures of the clusters shown in Figure 1 have all been determined from single crystal X-ray diffraction studies. However, characterizing cluster structures directly in solution, as is needed for in situ studies, is more challenging. Extended X-ray absorption fine structure (EXAFS) has been used to characterize the atomic structure of some small clusters[14a,16] and limited structural information can be obtained from Nuclear Magnetic Resonance (NMR) spectroscopy.[16b] However, these methods only provide information on the very local atomic range. Here, we use in situ X-ray total scattering (TS) and pair distribution function analysis[17] (PDF) to follow the formation of $[Bi_{38}O_{45}]$ from $[Bi_6O_8]$ as a model reaction for nanocluster formation and growth. As the Fourier transform of the TS signal, the PDF represents a histogram of all interatomic distances in a sample, and thus provide atomic structural information from the local to the global range. PDF is an excellent technique for in situ studies of materials formation in solution,[18] and has been applied to study a few large cluster systems previously[12a 16b] in order to characterize their solution structure, but not in situ to follow cluster reactions. While PDF analysis offers information on the atomic structure of matter, it is less sensitive to for example, cluster or particle size and shape. A way to complement the structural information available in the PDF is to combine the technique with small-angle X-ray scattering (SAXS), which provides information on the size, morphology and size dispersion of clusters or particles.[19]

We here use PDF and SAXS to study the formation of the $[Bi_{38}O_{45}]$ cluster starting from $[Bi_6O_5(OH)_3(NO_3)_5]\cdot 3H_2O$[8a] in dimethyl sulfoxide (DMSO) and obtain detailed information on the reaction pathway from octahedral $[Bi_6O_8]$ units to $[Bi_{38}O_{45}]$ nanoclusters. To analyze the data, we have developed an automated modeling approach[20] to identify intermediates and the reaction pathway. This automated approach, where all relevant smaller cluster structures, based on the $[Bi_{38}O_{45}]$ framework, is tested against the experimental PDF, allows us to readily identify the size and structure evolution during the reaction. Our results clearly identify $[Bi_{22}O_y]$ as a metastable intermediate structure in the reaction, and we do not observe $[Bi_6O_8]$ units as a reaction intermediate on the time scale of our experiments. We also demonstrate how PDF can be used to characterize restructuring effects of the solvent at the surface of nanoclusters and show that the cluster–solvent interaction affects the $[Bi_{38}O_{45}]$ clusters themselves, as it introduces disorder in their structure. This effect is highly dependent on the presence and type of the ligand covering the clusters. The methods and modeling tools developed here, using automated and combined SAXS and PDF analysis thus provides insights into cluster chemistry in solution.

Results and Discussion

Figure 2A shows in situ X-ray total scattering data obtained during the formation of $[Bi_{38}O_{45}]$ from $[Bi_6O_5(OH)_3(NO_3)_5]\cdot 3H_2O$ dissolved in DMSO. The experiment was done at $T = 80\,°C$, and data sets obtained from similar experiments performed at lower temperatures ($T =$ 30 °C–60 °C) can be found in Figure S1. At the beginning of the reaction, Bragg peaks from the crystalline $[Bi_6O_5(OH)_3(NO_3)_5]\cdot 3H_2O$ phase (Figure 2D) is seen, as crystals at this point are still in suspension in DMSO. After approximately 7 min, the crystals have fully dissolved, and only diffuse scattering is seen. We therefore turn to PDF for further structural analysis, and the corresponding PDFs are plotted in Figure 2B. The PDFs are the Fourier transformation of the TS data, where the signal from DMSO has been subtracted, as illustrated in Figure S2. In the beginning of the experiment (Figure 2E), the PDF shows the presence of long-range order from the crystalline starting material, and as expected, the data can be fitted with the $[Bi_6O_5(OH)_3(NO_3)_5]\cdot 3H_2O$ structure. Towards the end of the experiments the long-range order disappears, and the PDFs now show peaks up to only about 12 Å.

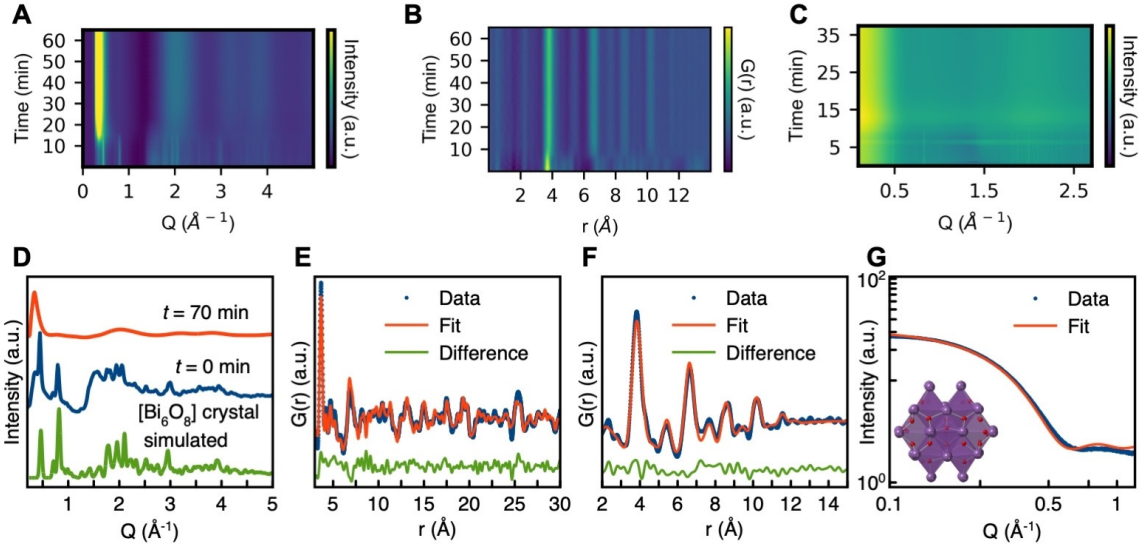

Figure 2. A) Background subtracted in situ X-ray TS data obtained during the experiment performed at $T=80\,°C$ plotted as a function of time. While Bragg peaks are seen at the beginning of the reaction, only diffuse features are seen after dissolution. B) Corresponding PDFs plotted as a function of time. C) Background subtracted SAXS data obtained during a similar experiment plotted as a function of time. The intensity is shown on a logarithmic scale. D) Simulated X-ray scattering data of the $[Bi_6O_5(OH)_3(NO_3)_5]\cdot 3\,H_2O$ crystal structure, compared to background subtracted data from $t=0$ min and $t=70$ min, $T=80\,°C$. E) Fit of the $[Bi_6O_5(OH)_3(NO_3)_5]\cdot 3\,H_2O$ crystal structure to the PDF obtained from the first frame in the experiment at $t=0$ min. $R_{wp}=29.0\,\%$. F) Fit of the $[Bi_{38}O_{45}]$ cluster structure to the PDF obtained at the end of the experiment at $t=70$ min; $R_{wp}=16.6\,\%$. G) Fit of the $[Bi_{38}O_{45}]$ cluster structure to the SAXS data obtained at the end of the experiment at $t=37$ min; $R_{wp}=3.1\,\%$. The SAXS data are plotted in a log–log plot.

In Figure 2F, the PDF obtained at the end of the experiment is fitted with the $[Bi_{38}O_{45}]$ model, confirming the product of the reaction. The cluster model (Figure 1D) was obtained from the structure of crystalline $[Bi_{38}O_{45}(NO_3)_{20}(DMSO)_{28}](NO_3)_4\cdot 4\,DMSO$,[4a] where an isolated $[Bi_{38}O_{45}]$ cluster was cut out of the crystal structure. The modeling (described in detail in Table S1) was set up so that the basic atomic structure was kept fixed during the refinement. The excellent fit illustrates that the structure of the $[Bi_{38}O_{45}]$ cluster in solution is similar (if not identical) to that seen in the crystalline phase, as also confirmed from DLS measurements (see Figure S3).

The presence of the $[Bi_{38}O_{45}]$ cluster at the end of the experiment is further supported by SAXS experiments. In situ SAXS data from a similar experiment are shown in Figure 2C. Bragg peaks from the crystalline $[Bi_6O_5(OH)_3(NO_3)_5]\cdot 3\,H_2O$ phase can again be identified at the beginning of the reaction (Figure 2C) but disappear after approximately 10 min. Figure 2G shows the SAXS data obtained at the end of the experiment fitted with the $[Bi_{38}O_{45}]$ cluster using the Debye equation as described in detail in Table S2. Again, the fits show excellent agreement between data and model.

Having established that we can use PDF and SAXS to confirm the starting point and end point of the reaction, we now move to characterize the structures seen during the cluster growth and identify intermediate species. Figure 3A shows selected PDFs from the process, clearly illustrating that a smaller cluster than $[Bi_{38}O_{45}]$ is present at the beginning of the reaction after dissolution. Initially, we had expected to see the presence of isolated $[Bi_6O_8]$ clusters in solution, since it is described as particularly stable.[9a,13] The calculated PDF from a $[Bi_6O_8]$ cluster is shown in Figure 3A showing only a few peaks from the small structure. Surprisingly, we cannot

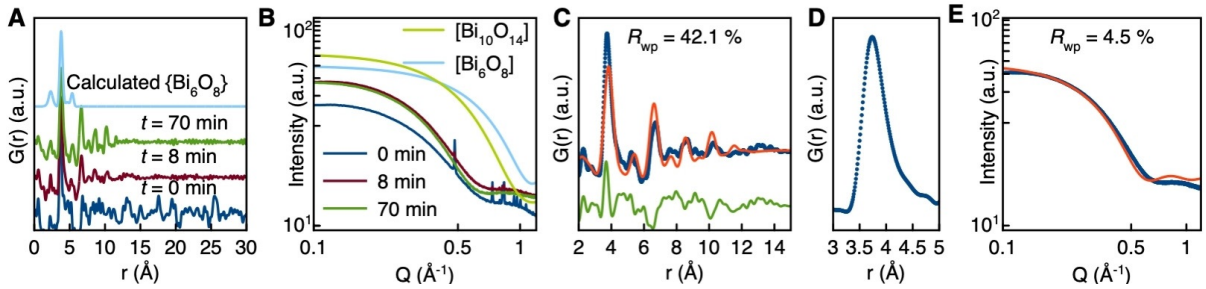

Figure 3. A, B) Comparison of experimental PDFs (A) and SAXS data (log–log plot) (B) with calculated patterns from an isolated $[Bi_6O_8]$ unit and a $[Bi_{10}O_{14}]$ "dimer". C) Fit of the $[Bi_{38}O_{45}]$ cluster structure to the PDF obtained after the dissolution of the crystalline starting material; $T=80\,°C$, $t=8$ min. D) Asymmetric peak at 3.8 Å in the PDF. E) A log–log plot of the fit of the $[Bi_{38}O_{45}]$ cluster structure to the SAXS data obtained after the dissolution of the crystalline precursor; $T=80\,°C$, $t=16$ min.

identify a PDF similar to this at any point in our in situ data from any reaction temperature, as peaks to higher r values are seen immediately after dissolution has occurred. This indicates that the small $[Bi_6O_8]$ clusters are not stable in DMSO on the time scales and experimental conditions of the in situ X-ray scattering experiments. This observation is confirmed by SAXS (Figure 3B), where isolated, monodisperse $[Bi_6O_8]$ clusters are not seen at any point in our data. We also do not observe the presence of for example, $[Bi_{10}O_{14}]$ structures (two edge-sharing $[Bi_6O_8]$ units) or any smaller fragments. While we cannot rule out that such structures are present in very small concentrations in the samples, they are not main species.

$[Bi_6O_8]$ was observed as a very dominant species in in situ ESI-MS experiments.[13] However, the conditions used for the ESI-MS measurements were different from the current scattering studies, as the hydrolysis reactions in the ESI-MS experiments were followed at room temperature, at much lower Bi concentration (0.05 mM–1 mM for ESI-MS vs. 230 mM for PDF/SAXS), and in a different solvent, namely a mixture of DMSO and dichloromethane, CH_2Cl_2. These highly different conditions may explain the differences in the species observed. However, ESI-MS is also more sensitive to minor species than both PDF and SAXS, although they will only be detected if they can easily be charged. The two experiments are thus not in contradiction but provide information for different conditions and different time scales: While the ESI-MS studies show that $[Bi_6O_8]$ species form rapidly after dissolution, their absence from our in situ X-ray scattering data indicate very low solubility and thus low concentration of these species and fast condensation after dissolution in DMSO. Both experiments show the formation of $[Bi_{22}O_{26}]$ clusters as quite stable intermediate and $[Bi_{38}O_{45}]$ as final products.

We can now analyze the structure of the intermediate species. From the similar PDF peak positions between the intermediate structure ($t = 8$ min) and the final cluster ($t =$ 70 min) seen in Figure 3A, it is evident that the intermediate is structurally related to the $[Bi_{38}O_{45}]$ cluster, as many of the main peaks show up in both PDFs. However, the peaks representing the largest interatomic distances are not present in the PDF from the intermediate cluster, which also appears to be significantly more disordered, as seen from the asymmetric broadening of the first Bi···Bi peak at $r = 3.8$ Å in Figure 3D. Figure 3C shows a fit of the $[Bi_{38}O_{45}]$ structure to the PDF from the intermediate cluster. In Figure 3E, the SAXS fit of the $[Bi_{38}O_{45}]$ cluster to data representing the intermediate confirm that the cluster is smaller than the final $[Bi_{38}O_{45}]$.

To characterize the cluster size evolution during the reaction, we first analyze the in situ SAXS data with a form factor analysis. Details on the modeling and examples of fits are given in Table S3 and Figure S4. The results (Figures S5 and S6) show that the average cluster size increases during the reaction, and the clusters present are of a higher size dispersity at the beginning of the reaction than at the end, where the presence of stable $[Bi_{38}O_{45}]$ clusters results in a very low size dispersity.

The observation that the intermediate cluster is smaller but structurally close to the $[Bi_{38}O_{45}]$ structure agrees well with the chemistry of bismuth oxido clusters discussed above, as several different sizes of bismuth oxido clusters, all built up from $[Bi_6O_8]$ units can be synthesized. We therefore attempted to fit other known cluster structures, with sizes between $[Bi_6O_8]$ to $[Bi_{38}O_{45}]$, to the intermediate PDF as shown in Figure S7. The best cluster candidates were the $[Bi_{18}O_{36}]$ and $[Bi_{22}O_{38}]$ structures, agreeing well with observations from in situ ESI-MS analysis, molecular dynamics simulations and quantum chemical calculations.[13,15a,b] However, to look further into the time-dependent structural changes, and to probe a larger structural space, we developed an automated method, where all smaller cluster structures based on the $[Bi_{38}O_{45}]$ framework were tested against the experimental PDF. Automated modeling methods for PDF analysis have recently been proposed by Banerjee et al.[21] for analysis of metal nanoparticles. In a recent study, we developed a method, where structural motifs in molybdenum oxide structures were identified by fitting automatically generated fragments of know polyoxometalate structures to PDFs.[20] We here apply an extension of this latter method to in situ data in order to identify intermediates and reaction pathways.

The principle is illustrated in Figure 4. First, the $[Bi_{38}O_{45}]$ model is fit to the PDF obtained from the last frame in the experimental series. It was thereafter tested whether a smaller version of the structure, i.e., with some Bi and O atoms removed would result in a better fit to the data, as described in more detail in the Supporting Information, section I.

This method can give us an overview of the best fitting structure (built up from edge-sharing $[Bi_6O_8]$ units) for every frame obtained during the reaction. Figure 5A–C shows the results from the automated modeling described above, where the refined number of Bi atoms is plotted as a function of time for the in situ experiments done at $T = 80$ °C, 60 °C, and 30 °C. Results from experiments done at other temperatures are given in Figure S8. Figure 5A–C firstly show that larger structures appear to be stabilized at higher reaction temperatures, and that the clusters grow with time. In Figure 5A ($T =$ 80 °C) plateaus at approximately 32 Bi atoms and 28 Bi atoms are identified, labelled as I and II. The same plateau at 28 Bi atoms is seen for the data obtained at $T = 60$ °C (Figure 5B), whereas data from $T = 30$ °C (Figure 5C) show plateaus at 25 and 20 Bi atoms (III and IV). The occurrence of clusters of a given size is illustrated in Figure 5D, which shows a histogram of the cluster structures identified in all three datasets. This shows that a large proportion of the identified clusters have between 20 and 25 Bi atoms. In Figure 6E–H, we show the structures I–IV along with fits to selected data. While these structures fit the data well, they appear unphysical, as "dangling" Bi atoms are seen. However, when looking closer, we identify that they share a stable backbone of 22 Bi atoms. This is particularly clear for cluster III and IV, as seen in Figure 6A, where the Bi positions of these are compared to the $[Bi_{22}O_{26}]$ structure, and fits of the $[Bi_{22}O_{26}]$ cluster to the same frames (Figure 6B,C) are reasonable.

The results from the automated modeling thus indicate that $[Bi_{22}O_{26}]$ is an important intermediate in the reaction. We also saw other frequent sizes, such as Bi_{28} and Bi_{32}. However, these structures do not appear as closed-shell, physical structures, and are unlikely to be stable. The SAXS form

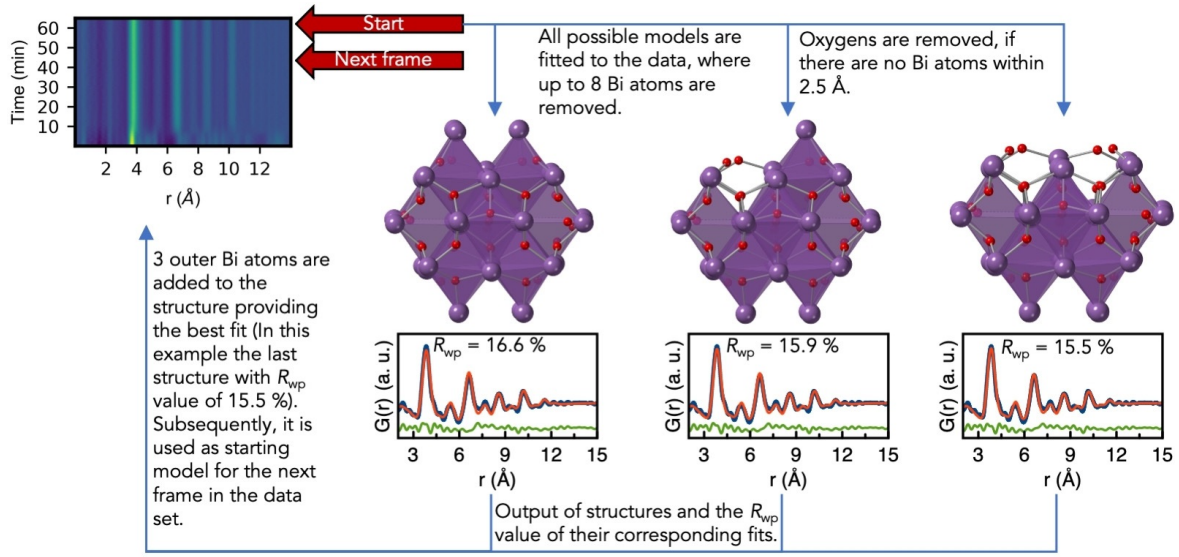

Figure 4. Sketch of the automated modeling process. The last frame of the in situ dataset is modeled with the $[Bi_{38}O_{45}]$ cluster structure and all structures in which up to 8 Bi atoms from the outer shell have been removed together with nonbonding oxygen atoms. The best fitting structure (with three Bi atoms added) is used as a starting point for the fitting of the second-last frame. This process is repeated for all frames in the reaction.

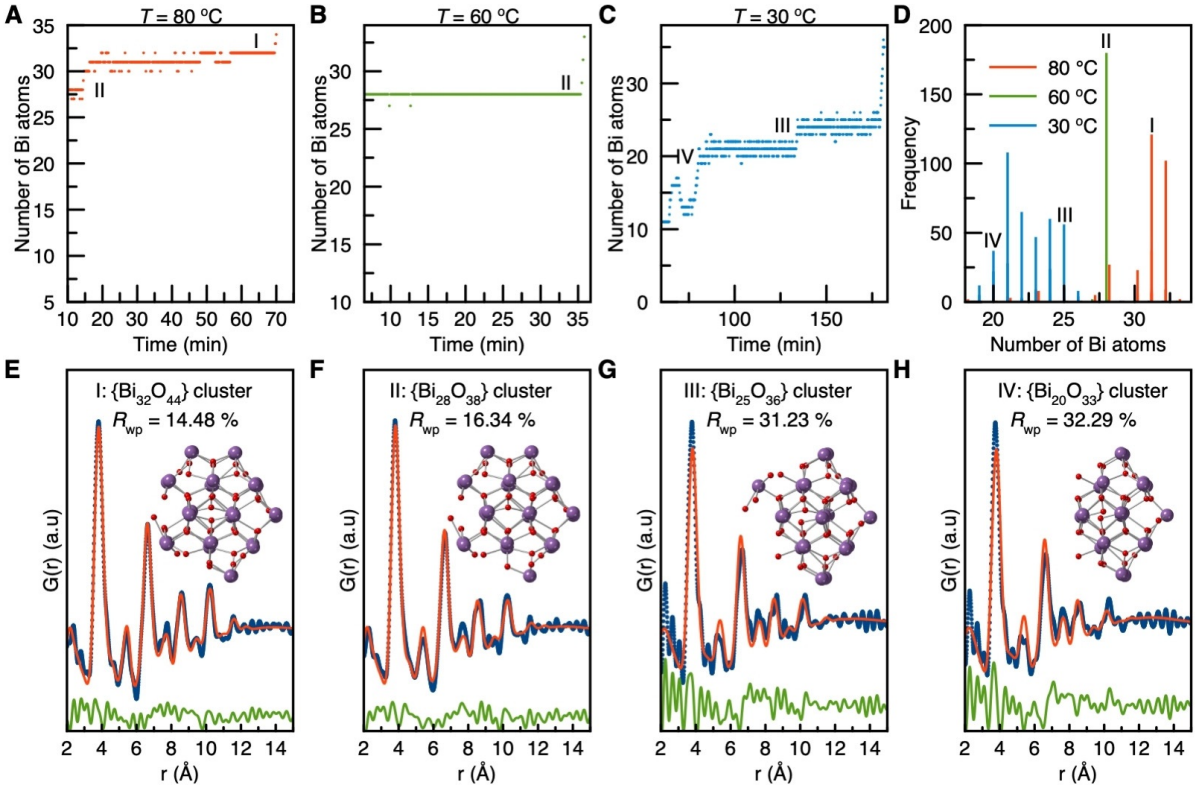

Figure 5. A–C) The number of bismuth atoms in the best fitting structure for each frame is plotted versus reaction time for the experiments done at $T = 80$, 60, and 30 °C. D) Histogram representing the number of Bi atoms in the best fitting structure through the reaction. Frequency is the number of times the specific cluster size is present during the reaction. E–H) Clusters and fits that have been obtained in the automated modeling process.

factor analysis described above (Figures S5 and S6) furthermore showed that before the reaction finished, a larger size dispersion is seen, thus indicating that multiple cluster sizes can be present during the reaction. We therefore tried fitting both the PDF and SAXS data with a two-structure model with the $[Bi_{22}O_{26}]$ and $[Bi_{38}O_{45}]$ clusters. The refined parameters are given in Tables S4–7 and the fits to both SAXS and PDF data are shown in Figure S9, where they are compared to the

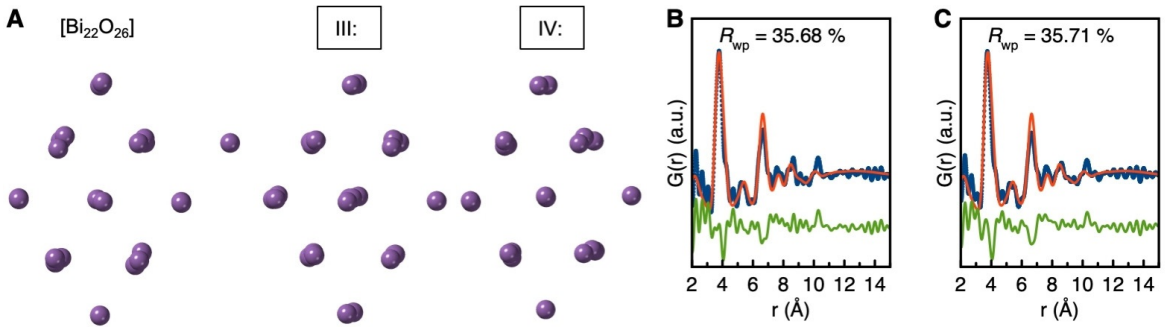

Figure 6. A) Comparison of the Bi positions in the $[Bi_{22}O_{26}]$ cluster with those of structures III and IV, found from the automated modeling method. B,C) Fit to the in situ PDF ($T = 30\,°C$) obtained at $t = 152$ min (B) and $t = 103$ min (C) using the $[Bi_{22}O_{26}]$ cluster as the model.

results from the automated modeling. In section K in the Supporting Information, we compare simulated SAXS data of the $[Bi_{22}O_{26}]$ and $[Bi_{38}O_{45}]$ clusters to data at two different time points in the reaction and compare two-phase SAXS refinements to fits using individual $[Bi_{22}O_{26}]$ and $[Bi_{38}O_{45}]$ clusters. Generally, the two-structure models provide similar fit qualities or better.

Having established that the main species present throughout the reaction are $[Bi_{22}O_{26}]$ and $[Bi_{38}O_{45}]$, we can sequentially analyze the data to extract phase fractions of the two clusters as a function of time. The results from this analysis are shown in Figure 7 (see Figure S12 for results from other reaction temperatures). Results from SAXS is shown in blue, and PDF in red, illustrating how the $[Bi_{38}O_{45}]$ fraction increases with function of time and temperature. Analysis of SAXS and PDF data independently show similar phase fractions of the two clusters in the high temperature cases, and the amount of the $[Bi_{38}O_{45}]$ cluster steadily increases. We therefore attempted a combined analysis method, that is, using the so-called complex modeling approach.[19b–d,22] Complex modeling using SAXS and PDF analysis has been exemplified for CdS nanoparticles, where Farrow et al.[19b] showed that by combining the two techniques, a much more robust description of particle size and shape could be obtained. Here, we have in a similar way used the program Diffpy-CMI for complex modeling of PDF and SAXS data. However, we have applied the Debye equation to calculate the scattering pattern in both the SAXS regime and PDF regime, as described in detail in the Supporting Information, sections L and M. The results of the combined modeling are shown in green in Figure 7 and generally agree well with the individual SAXS and PDF analysis, but with more certainty on the refined parameters as seen from the less scattered data points.

While the results from the experiments done at higher temperatures ($T = 50\,°C$–$80\,°C$) generally show clear trends and a good agreement between the SAXS and PDF results, larger discrepancies are observed for the data seen from experiments done at lower temperatures, illustrated for $T = 30\,°C$ in Figure 7C. Here, the PDF results are somewhat scattered, while the SAXS refinements appear to give a clearer trend. The dispersity analysis illustrated in Figures S5 and S6 furthermore showed a larger dispersion of sizes for low temperature experiments, and it may be that small fractions of other cluster structures or fragments are present for longer times during these slower reactions.

The data indicate that in none of the experiments, a full reaction to $[Bi_{38}O_{45}]$ takes place, as some $[Bi_{22}O_{26}]$ is present at the end of the experiment. The refined fraction of the final $[Bi_{38}O_{45}]$ cluster is approximately 60 % at the end of the in situ experiment at $T = 80\,°C$, and for the reactions done at lower temperatures, the $[Bi_{22}O_{26}]$ cluster remains the majority species in the solution. However, PDF and SAXS data collected from samples kept up to 275 days at room temperature show excellent fits with a single phase $[Bi_{38}O_{45}]$ model (Figures S16 and S18).

Combined, the results from the automated PDF analysis and the complex modeling of SAXS and PDF data allow us to establish the overall reaction route. When $[Bi_6O_5(OH)_3(NO_3)_5]\cdot 3H_2O$ is dissolved in DMSO, larger clusters quickly form, and we never observe free $[Bi_6O_8]$ (or smaller structure fragments) in our data at a time resolution

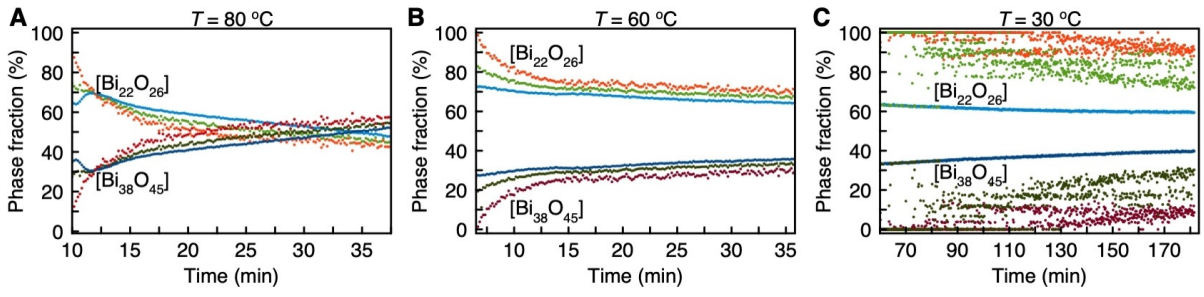

Figure 7. Phase fractions of the $[Bi_{22}O_{26}]$ and $[Bi_{38}O_{45}]$ clusters, plotted as a function of time for experiments at A) $T = 80\,°C$, B) 60 °C, and C) 30 °C. Results from PDF are plotted in red, from SAXS in blue, and from complex modeling in green.

of 4 s. This process most likely takes place through condensation reactions and rearrangement processes, as also suggested by Sattler et al.[13] The main intermediate species we observe is $[Bi_{22}O_{26}]$, as concluded from both SAXS and PDF data. This cluster is quite stable and co-exists with $[Bi_{38}O_{45}]$ in the time range investigated with in situ experiments. The local structure changes taking place during dissolution are discussed further in the Supporting Information, section O. The experiments discussed so far were all done from $[Bi_6O_5(OH)_3(NO_3)_5]\cdot 3H_2O$. Nearly identical results were obtained when the starting crystalline material was changed to $[Bi_6O_4(OH)_4(NO_3)_6(H_2O)_2]\cdot(H_2O)$ (see Figure S18). This indicates that the results presented are general for compounds based on a hexanuclear bismuth oxido core $[Bi_6O_8]$ dissolved in DMSO.

Using SAXS and PDF, we have identified the main intermediate species in the process. Nevertheless, some questions regarding the cluster growth remain unanswered from the current study. As discussed above, it has previously been suggested that cluster growth takes place through oligomerization reactions involving fragments of $[Bi_6O_8]$ units as key species. Our data and time resolution do not allow us to identify these short-lived species or the specific mechanism. Several processes may take place in the reaction: for example, elusive, larger intermediates assembled from $[Bi_6O_8]$ units may form, which could collapse or partly dissociate to result in the $[Bi_{22}O_{26}]$ structure. Dissociation of $[Bi_6O_8]$ fragments could also take place before oligomerization to lead stepwise to $[Bi_{22}O_{26}]$ and finally to $[Bi_{38}O_{45}]$. This hypothesis is supported by ESI-MS studies of the hydrolysis of bismuth carboxylates, which revealed intermediates between Bi_3- and Bi_{13}-oxido clusters. Independent analytic techniques to support their formation in solution are missing, but several single crystal X-ray structures of other polynuclear bismuth oxido clusters including at least one $[Bi_6O_8]$ unit with various ligands have been reported.[9a,15c] The time resolution for the scattering experiments currently possible limits our insight into the fast processes in solution; for example, molecular dynamic simulations have suggested that the growth from $[Bi_6O_8]$ units take place on the nanosecond to microsecond time scale.[15a] In the future, new possibilities for ultrafast, high flux X-ray scattering studies may open for studies of such processes.[23] If one could chemically stabilize a series of species formed on the way to the $[Bi_{22}O_{26}]$ clusters, new insight could also be obtained.

Ligand Exchange: From $[Bi_{38}O_{45}(NO_3)_{20}(DMSO)_\delta]$ to $[Bi_{38}O_{45}(OMc)_{24}(DMSO)_\delta]$

PDF analysis also allows us to study cluster–solvent interactions and any structural changes that may take place during exchange of ligands in the clusters. Figure 8A shows PDFs obtained when heating a solution of $[Bi_{38}O_{45}(NO_3)_{20}(DMSO)_{28}](NO_3)_4\cdot 4DMSO$ in DMSO with sodium methacrylate. In this process, nitrate ligands are substituted with methacrylate[5,9a] making the clusters soluble in organic solvents. After 7 min of the reaction, significant changes appear. Figure 8B shows selected PDFs obtained over the course of the reaction. At the beginning, both the peaks at $r \approx 3.8$ Å and $r \approx 6.7$ Å have shoulders which disappear through the ligand exchange, and all of the peaks become narrower and more symmetric as the reaction progresses.

We start by modeling the first frame of the reaction with the $[Bi_{38}O_{45}]$ cluster structure, Figure 9A. While this model fits all main PDF peaks, significant misfits are seen, and the difference curve is similar to an exponentially dampened sinusoidal function. This behavior has previously been described by Zobel et al., who related it to solvent restructuring effects on the surface of nanoparticles.[24] Figure 9B shows the fit if a dampened sinusoidal function is added to the $[Bi_{38}O_{45}]$ model. This significantly improves the fit to the data, suggesting a strong interaction between the cluster (or its ligands) and the DMSO solvent. A PDF obtained from pure DMSO is shown in Figure S19 confirming that the oscillation does not arise from the solvent itself.

At the end of the reaction, the data (Figure 9D) is very well described by the $[Bi_{38}O_{45}]$ cluster, giving a R_{wp} value of 12.2%. Here, the exponential dampened sinusoidal does not contribute to the fit as seen in Figure 9E. Figure 9C (bottom) shows the R_{wp} values of the fits during the reaction. This behavior indicates that the structuring of the solvent dominates at the beginning of the reaction but when the ligand is exchanged to methacrylate, the effect vanishes. This is also clear when plotting the contribution of the dampened sinusoidal oscillation through the reaction, Figure 9F.

The ligand exchange, and the solvent interactions also appear to affect the atomic structure of the bismuth oxido clusters. Figure 9C (top) shows the refined ADPs of the Bi atoms through the reaction. This parameter relates to the width of the PDF peaks, and decreases through the reaction,

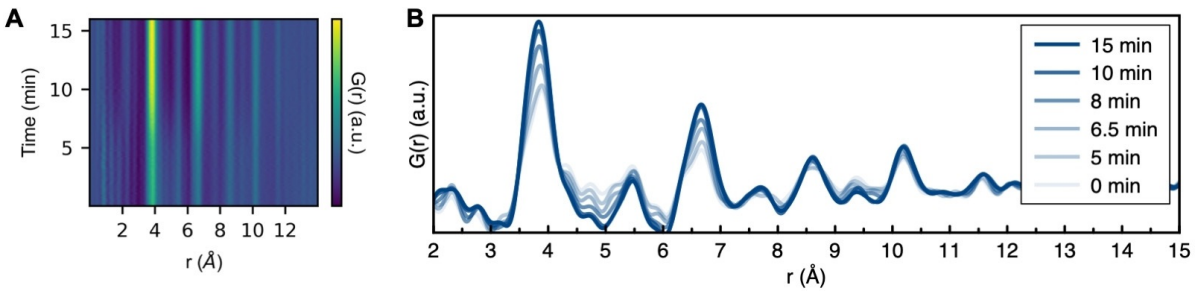

Figure 8. A) PDFs obtained from in situ X-ray TS data collected during the ligand-exchange experiment performed at $T = 80$ °C, plotted as a function of time. B) Selected PDFs from the experiment.

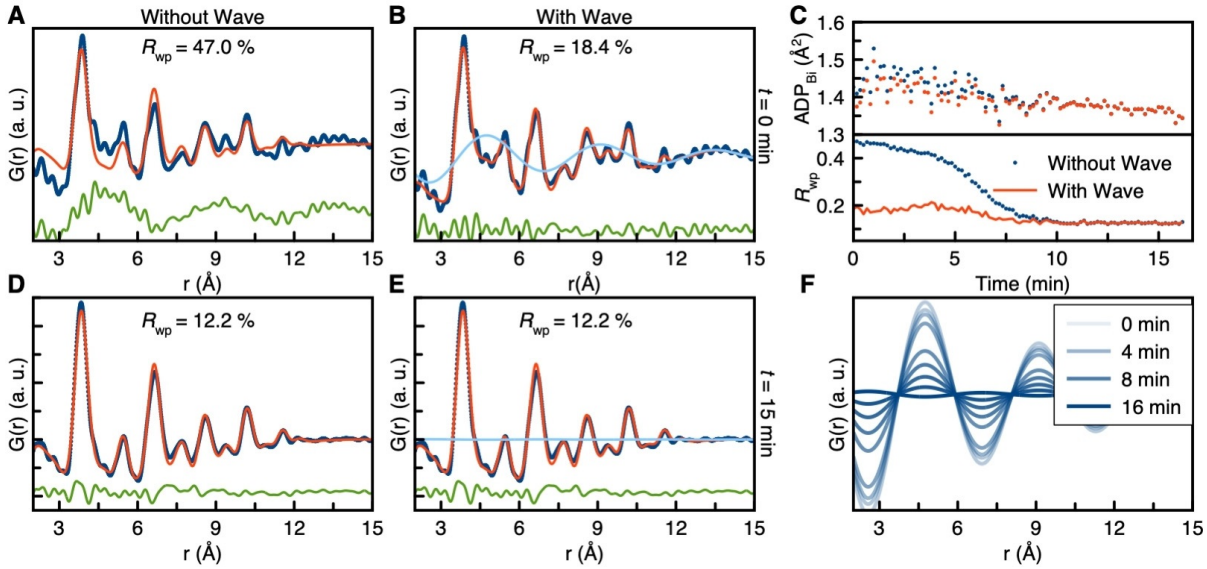

Figure 9. Representative fit of a PDF obtained during ligand exchange, obtained $t = 0$ min into the ligand-exchange reaction A) without including solvent restructuring effects (wave), B) including solvent restructuring effects (wave). C) R_{wp} values and ADP values of Bi obtained when modeling the time-resolved PDFs, obtained during ligand exchange, with the $[Bi_{38}O_{45}]$ model. D) Representative fit of a PDF obtained during ligand exchange, obtained $t = 15$ min into the reaction without including solvent restructuring effects and E) when including solvent restructuring effects at the surface of the nanocluster. F) The contribution of the solvent restructuring effects during the ligand-exchange reaction.

showing that the ligand-exchanged clusters with methacrylate are more ordered. The PDFs obtained from the beginning of the reaction furthermore show highly asymmetric peaks, as seen most clearly from the shoulder peak at about 4.2 Å. This asymmetry is likely to be an effect of the strong interaction between the cluster and the DMSO solvent. Modeling details are given in Table S8,9.

The solvent restructuring in the beginning of the reaction is likely due to partial dissociation of nitrate ligands, which results in a cationic cluster, making the coordination to DMSO strong. This can result in some distortion of the $[Bi_{38}O_{45}]$ core as seen from PDF peaks asymmetry. When the nitrate ligand is substituted with methacrylate, the strong bonding between methacrylate and the $[Bi_{38}O_{45}]$ clusters hamper the coordination of DMSO to the nanoclusters, and the effect in the PDF vanishes. This is also reflected when considering the crystal structures of $[Bi_{38}O_{45}(NO_3)_{20}(DMSO)_{28}](NO_3)_4{\cdot}4DMSO$[4a] and $[Bi_{38}O_{45}(OMc)_{24}(DMSO)_9]{\cdot}2DMSO{\cdot}7H_2O$:[5] For the nitrate-coordinated cluster, 28 DMSO molecules coordinate to the bismuth oxido core, while this is only 9 for the crystal structure containing methacrylate.

A sketch of how the solvent restructures at the surface of the $[Bi_{38}O_{45}]$ clusters is illustrated in Figure 10. The DMSO molecules coordinate to the nanocluster through strong bonding to the surface of the bismuth oxido cluster with directions perpendicular to the surface of the $[Bi_{38}O_{45}]$ clusters. This results in regions with alternating low and high electron density due to packing of solvent molecules. Collectively, this gives rise to a sinusoidal oscillation contributing to the PDF. Since the solvent effect is strongest close to the surface of the $[Bi_{38}O_{45}]$ clusters and it slowly transforms into a bulk solvent structure of DMSO, the sinusoidal oscillation exponentially decays. However, we observe solvent effects of up to $r = 30$ Å.

Conclusion

In situ PDF and SAXS have been used to follow the reaction from a suspension of $[Bi_6O_5(OH)_3(NO_3)_5]{\cdot}3H_2O$ in DMSO to $[Bi_{38}O_{45}]$ clusters in solution (Figure 11). The structural modeling was done using the Debye equation, and we applied combined modeling of the PDF and SAXS data. To follow the cluster growth taking place during the reaction, we introduced an automated modeling method, where intermediate species were identified by iteratively removing atoms from the final $[Bi_{38}O_{45}]$ structure. This analysis showed that starting from $[Bi_6O_8]$ a $[Bi_{22}O_{26}]$ intermediate very quickly forms and slowly transforms to $[Bi_{38}O_{45}]$. The formation of the $[Bi_{22}O_{26}]$ structure unexpectedly proceeded immediately after dissolution of the crystalline starting material, meaning that the time resolution of the X-ray scattering experiments does not allow us to identify any short-lived building blocks that may form before the larger clusters are seen. Questions regarding e.g., oligomerization reactions and cluster fragmentation thus remain open, but the combination of SAXS and PDF provided new insight into the cluster growth process of bismuth oxido species including information on the time scale at which processes occur.

We furthermore demonstrate that due to nitrate ligand dissociation, a strong interaction between DMSO and the bismuth oxido clusters induce restructuring of solvent molecules around the bismuth oxido clusters. This interaction leads to disorder of the atomic structure in the bismuth oxido clusters themselves, as seen from the width and asymmetry of PDF peaks. When methacrylate is introduced as a ligand in

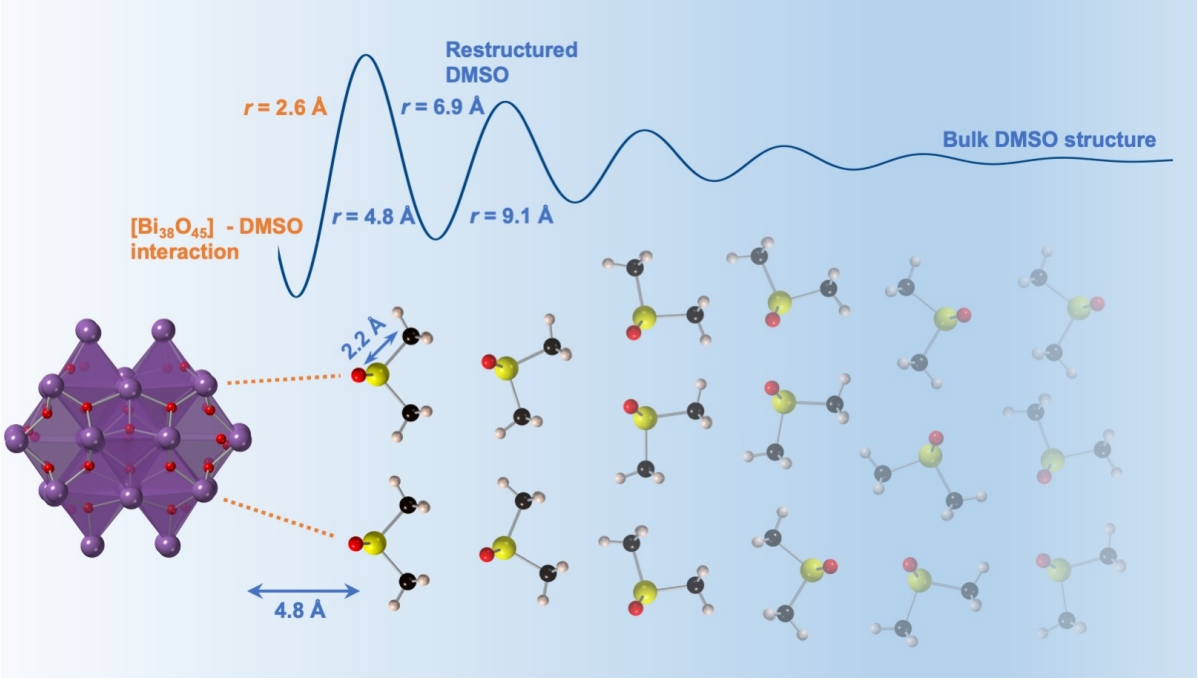

Figure 10. Illustration of how the surface of the $[Bi_{38}O_{45}]$ cluster, with nitrate as the ligand, induces a solvent restructuring effect up to $r = 30$ Å. Interactions between the bismuth oxido clusters and the DMSO molecules induce an ordering of the solvent molecules near the $[Bi_{38}O_{45}]$ cluster surface, which gives rise to an exponentially dampened sinusoidal oscillation in the PDF. Carbon atoms are shown in black, sulfur in yellow, and hydrogen in beige.

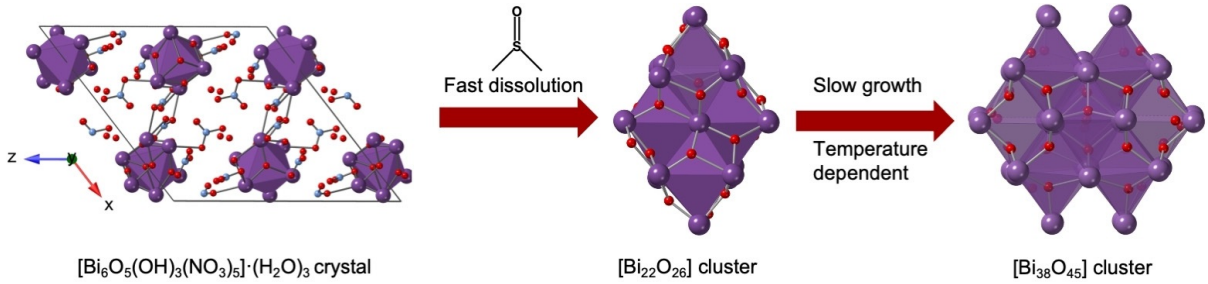

Figure 11. The $[Bi_6O_5(OH)_3(NO_3)_5]\cdot 3\,H_2O$ crystals dissolve in DMSO to form a $[Bi_{22}O_{26}]$ cluster as an intermediate before forming atomically precise $[Bi_{38}O_{45}]$ clusters.

the $[Bi_{38}O_{45}]$ cluster, it screens the cluster from strong solvent interactions, consequently leaving the $[Bi_{38}O_{45}]$ core more ordered and closer to that observed in the crystalline structure. However, the $[Bi_{38}O_{45}]$ core structure stays intact during the ligand substitution reaction, which demonstrates that such atomically precise metal oxido nanoclusters can serve as model structures to study ligand effects at the surface of metal oxide nanoparticles.

The chemical knowledge built up in this study is likely transferable to the growth of other metal oxido clusters, at least to metal oxides of the fluorite type such as uranium, cerium and plutonium oxido nanoclusters, which also show a stable nuclearity of 38 metal atoms in their cluster core. The insights that can be obtained from combined in situ X-ray scattering studies furthermore open for understanding material formation in solution. For example, SAXS and PDF studies may allow the identification of prenucleation clusters, and provide a much deeper understanding of the fundamental processes involved in nucleation. Studies of atomically monodisperse metal oxido cluster structures, as done here, can furthermore provide knowledge of metal oxide chemistry, and it is likely that the metastable $[Bi_{22}O_{26}]$ cluster observed here may be an important species in bismuth oxide formation. Understanding the solution chemistry of metal oxido clusters on an atomic and molecular scale can thus open new opportunities for synthesizing nanoscale metal oxides in a controlled manner.

Acknowledgements

This work is part of a project that has received funding from the European Research Council (ERC) under the European Union's Horizon 2020 Research and Innovation Programme (grant agreement No. 804066). We furthermore thank DANSCATT (supported by the Danish Agency for Science and

Higher Education) for support. A.S.A. acknowledges the Siemens Foundation for support for his thesis project. We acknowledge DESY (Hamburg, Germany), a member of the Helmholtz Association HGF, for the provision of experimental facilities. Parts of this research were carried out at beamline P02.1 and P07 at Petra III, and we thank Martin Etter, Jozef Bednarcik and Ann-Christin Dippel for assistance in using the beamline. We acknowledge SOLEIL for provision of synchrotron radiation facilities, and we thank Thomas Bizien for assistance in using beamline SWING. We acknowledge the European Synchrotron Radiation Facility for provision of synchrotron radiation facilities, and we thank Peter Boesecke for assistance in using beamline ID02. We thank the Deutsche Forschungsgemeinschaft (DFG SPP1415: Crystalline Nonequilibrium Phases—Preparation, Characterization and in situ Studies of Formation Mechanisms; ME 2284/3-2) for support. M.S. and E.B. acknowledge the Innovation Fund Denmark (IFD) as part of project Linking Industry to Neutrons and X-rays (LINX) under File No. 5152-00005B for partly funding this project. Open access funding enabled and organized by Projekt DEAL.

Conflict of Interest

The authors declare no conflict of interest.

Keywords: bismuth · in situ studies · nanostructures · pair distribution function · small-angle X-ray scattering

[1] E. D. Bøjesen, B. B. Iversen, *CrystEngComm* **2016**, *18*, 8332 – 8353.
[2] a) P. D. Matthews, T. C. King, D. S. Wright, *Chem. Commun.* **2014**, *50*, 12815 – 12823; b) P. Coppens, Y. Chen, E. Trzop, *Chem. Rev.* **2014**, *114*, 9645 – 9661; c) W.-H. Fang, L. Zhang, J. Zhang, *J. Am. Chem. Soc.* **2016**, *138*, 7480 – 7483; d) S. Yang, H.-C. Su, J.-L. Hou, W. Luo, D.-H. Zou, Q.-Y. Zhu, J. Dai, *Dalton Trans.* **2017**, *46*, 9639 – 9645; e) P. D. Matthews, N. Li, H.-K. Luo, D. S. Wright, *Chem. Eur. J.* **2016**, *22*, 4632 – 4633.
[3] a) K. J. Mitchell, K. A. Abboud, G. Christou, *Nat. Commun.* **2017**, *8*, 1445; b) B. Russell-Webster, K. A. Abboud, G. Christou, *Chem. Commun.* **2020**, *56*, 5382 – 5385.
[4] a) L. Miersch, T. Rüffer, M. Schlesinger, H. Lang, M. Mehring, *Inorg. Chem.* **2012**, *51*, 9376 – 9384; b) F. Y. Du, J. M. Lou, R. Jiang, Z. Z. Fang, X. F. Zhao, Y. Y. Niu, S. Q. Zou, M. M. Zhang, A. H. Gong, C. Y. Wu, *Int. J. Nanomed.* **2017**, *12*, 5973 – 5992.
[5] L. Miersch, T. Rüffer, M. Mehring, *Chem. Commun.* **2011**, *47*, 6353 – 6355.
[6] M. Schlesinger, S. Schulze, M. Hietschold, M. Mehring, *Dalton Trans.* **2013**, *42*, 1047 – 1056.
[7] M. Weber, M. Schlesinger, M. Mehring, *Cryst. Growth Des.* **2016**, *16*, 5678 – 5688.
[8] a) F. Lazarini, *Acta Crystallogr.* **1978**, *34*, 3169 – 3173; b) D. L. Rogow, H. Fei, D. P. Brennan, M. Ikehata, P. Y. Zavalij, A. G. Oliver, S. R. J. Oliver, *Inorg. Chem.* **2010**, *49*, 5619 – 5624; c) M. Mehring, S. Paalasmaa, M. Schürmann, *Eur. J. Inorg. Chem.* **2005**, 4891 – 4901; d) M. Mehring, D. Mansfeld, S. Paalasmaa, M. Schürmann, *Chem. Eur. J.* **2006**, *12*, 1767 – 1781; e) D. Mansfeld, M. Mehring, M. Schürmann, *Angew. Chem. Int. Ed.* **2005**, *44*, 245 – 249; *Angew. Chem.* **2005**, *117*, 250 – 254; f) X. Kou, X. Wang, D. Mendoza-Espinosa, L. N. Zakharov, A. L. Rheingold, W. H. Watson, K. A. Brien, L. K. Jayarathna, T. A. Hanna, *Inorg. Chem.* **2009**, *48*, 11002 – 11016; g) M. Weber, T. Rüffer, F. Speck, F. Göhler, D. P. Weimann, C. A. Schalley, T. Seyller, H. Lang, M. Mehring, *Inorg. Chem.* **2020**, *59*, 3353 – 3366.
[9] a) M. Mehring in *Clusters—Contemporary Insight in Structure and Bonding* (Ed.: S. Dehnen), Springer International Publishing, Cham, **2017**, pp. 201 – 268; b) M. Mehring, *Coord. Chem. Rev.* **2007**, *251*, 974 – 1006.
[10] I. L. Malaestean, A. Ellern, S. Baca, P. Kogerler, *Chem. Commun.* **2012**, *48*, 1499 – 1501.
[11] C. Falaise, C. Volkringer, J. F. Vigier, A. Beaurain, P. Roussel, P. Rabu, T. Loiseau, *J. Am. Chem. Soc.* **2013**, *135*, 15678 – 15681.
[12] a) L. Soderholm, P. M. Almond, S. Skanthakumar, R. E. Wilson, P. C. Burns, *Angew. Chem. Int. Ed.* **2008**, *47*, 298 – 302; *Angew. Chem.* **2008**, *120*, 304 – 308; b) R. E. Wilson, S. Skanthakumar, L. Soderholm, *Angew. Chem. Int. Ed.* **2011**, *50*, 11234 – 11237; *Angew. Chem.* **2011**, *123*, 11430 – 11433.
[13] D. Sattler, M. Schlesinger, M. Mehring, C. A. Schalley, *ChemPlusChem* **2013**, *78*, 1005 – 1014.
[14] a) K. Takao, S. Takao, A. C. Scheinost, G. Bernhard, C. Hennig, *Inorg. Chem.* **2012**, *51*, 1336 – 1344; b) S. Takao, K. Takao, W. Kraus, F. Emmerling, A. C. Scheinost, G. Bernhard, C. Hennig, *Eur. J. Inorg. Chem.* **2009**, 4771 – 4775; c) S. L. Estes, M. R. Antonio, L. Soderholm, *J. Phys. Chem. C* **2016**, *120*, 5810 – 5818.
[15] a) M. Walther, D. Zahn, *Eur. J. Inorg. Chem.* **2015**, 1178 – 1181; b) M. Walther, D. Zahn, *Chem. Phys. Lett.* **2018**, *691*, 87 – 90; c) M. Schlesinger, A. Pathak, S. Richter, D. Sattler, A. Seifert, T. Rüffer, P. C. Andrews, C. A. Schalley, H. Lang, M. Mehring, *Eur. J. Inorg. Chem.* **2014**, 4218 – 4227.
[16] a) C. Hennig, A. Ikeda-Ohno, W. Kraus, S. Weiss, P. Pattison, H. Emerich, P. M. Abdala, A. C. Scheinost, *Inorg. Chem.* **2013**, *52*, 11734 – 11743; b) Y.-J. Hu, K. E. Knope, S. Skanthakumar, L. Soderholm, *Eur. J. Inorg. Chem.* **2013**, 4159 – 4163; c) C. Hennig, S. Takao, K. Takao, S. Weiss, W. Kraus, F. Emmerling, A. C. Scheinost, *Dalton Trans.* **2012**, *41*, 12818 – 12823.
[17] S. J. L. Billinge, M. G. Kanatzidis, *Chem. Commun.* **2004**, 749 – 760.
[18] K. M. Ø. Jensen, C. Tyrsted, M. Bremholm, B. B. Iversen, *ChemSusChem* **2014**, *7*, 1594 – 1611.
[19] a) S. J. L. Billinge, I. Levin, *Science* **2007**, *316*, 561 – 565; b) C. Farrow, C. Shi, P. Juhás, X. Peng, S. J. L. Billinge, *J. Appl. Crystallogr.* **2014**, *47*, 561 – 565; c) P. Juhás, C. L. Farrow, X. Yang, K. R. Knox, S. J. L. Billinge, *Acta Crystallogr. Sect. A* **2015**, *71*, 562 – 568; d) C. L. Farrow, S. J. L. Billinge, *Acta Crystallogr. Sect. A* **2009**, *65*, 232 – 239.
[20] T. L. Christiansen, E. T. S. Kjær, A. Kovyakh, M. L. Röderen, M. Høj, T. Vosch, K. M. Ø. Jensen, *J. Appl. Crystallogr.* **2020**, *53*, 148 – 158.
[21] S. Banerjee, C.-H. Liu, J. D. Lee, A. Kovyakh, V. Grasmik, O. Prymak, C. Koenigsmann, H. Liu, L. Wang, A. M. M. Abeykoon, S. S. Wong, M. Epple, C. B. Murray, S. J. L. Billinge, *J. Phys. Chem. C* **2018**, *122*, 29498 – 29506.
[22] a) M. G. Tucker, D. A. Keen, M. T. Dove, A. L. Goodwin, Q. Hui, *J. Phys. Condens. Matter* **2007**, *19*, 335218; b) V. Krayzman, I. Levin, M. G. Tucker, *J. Appl. Crystallogr.* **2008**, *41*, 705 – 714.
[23] P. Fromme, *Nat. Chem. Biol.* **2015**, *11*, 895 – 899.
[24] a) M. Zobel, R. B. Neder, S. A. J. Kimber, *Science* **2015**, *347*, 292 – 294; b) S. L. J. Thomä, S. W. Krauss, M. Eckardt, P. Chater, M. Zobel, *Nat. Commun.* **2019**, *10*, 995.

Manuscript received: March 14, 2021
Accepted manuscript online: May 30, 2021
Version of record online: July 1, 2021

